

Experimental Testing of Rotor-Stator Contact in a Coupled Double Rotor System

Rafael Sánchez Crespo*, Alexander D. Shaw*, and Alan R. Champneys**

*College of Engineering, Swansea University, Swansea, United Kingdom

**Department of Engineering Mathematics, University of Bristol, Bristol, United Kingdom

Summary. The nonlinear vibrations due to rotor-stator contact show a variety of phenomena that are not well understood, particularly in rotors with higher degrees of freedom. Recent work suggests many responses involving intermittent contact between the rotor and stator are explain by internal resonance when the system is seen in a rotating coordinate frame. Different forms of internal resonance can be activated by varying the drive speed. This work seeks to predict these phenomena by comparing experimental testing results with numerical simulation results. The rotor-stator impacts in rotating machines can cause significant damage or failure in many industrial applications of turbomachinery, this work is relevant to systems with long flexible rotors.

Introduction

In many industrial applications, such as oil drilling, airplane engine, helicopter engine, and Jeffcott rotors, the rotor-stator impact or rubbing forces may occur due to a mass imbalance of the rotor or misalignment of defective bearings leading to damage or failure. The lateral displacements on rotating machines are caused by centrifugal forces, generated by a mass imbalance, introduced during the fabrication process of the components or as an undesirable product of assembly. Reducing these lateral displacements is one of the main goals in the vibrations control of rotating machines, according to [1]. Considerable research has been carried out on nonlinear rotor systems with an out of balance mass, such as [2] and [3].

Until now this research is the first to predict the asynchronous partial contact motion phenomena on a double rotor system by developing a mathematical model and conducting experimental testing to validate the simulation results. This research is the continuation of the work developed in [4], where a model of a shaft with two asymmetrically, non-identical discs is mounted on pinned bearings at each end, with a snubber ring mounted at the center of the shaft with a fixed clearance is derived using the finite-element method. The shaft is represented by a Timoshenko beam elements and the discs by additional inertia terms at the nodes. In [5] a mathematical model is developed for an oxygen pump in an aerospace engine with elastic supports and step-diameter hollow shaft considering the dynamic response due to contact. The simulation results demonstrated the grazing bifurcation causes a periodic motion to become quasi-periodic when contact starts.

The objective of this research is to predict the chattering or whirling of a rotor-stator contact motion in rotating machines using an experimental test rig to compare the results obtained with a mathematical model. The equations of motion predict multiple solutions at certain drive speeds, corresponding to different interactions between the modes of the underlying linear system.

Mathematical and experimental model

This research presents a mathematical model of a double rotor system with a length represented by L_1 and L_2 which are joined together by isotropic couplings having linear angular stiffness and damping k_{r1}, k_{r2}, c_{r1} and c_{r2} respectively, both rotors have a disc of mass M_1 and M_2 position at a specific length of each rotor, where b is the length measured from the excitation point where the motor is attached to the geometrical center of disc 1 and disc 2 is position at the end of rotor 2 at the geometrical center of disc 2, as shown in **Figure 1**. Each disc has a diameter d_1 and d_2 with a thickness v_1 and v_2 . The system is subjected to a radial clearance c of a stator in the form of snubber ring fixed with a linear spring system represented by k_s , positioned at length a measured from the geometrical center of disc 2 to the center of the snubber ring. The inertial reference frame xyz is positioned at the origin O , where the motor provides the rotational speed to the system and the subscript $i=1,2$ represents the coordinates of disc 1 and 2.

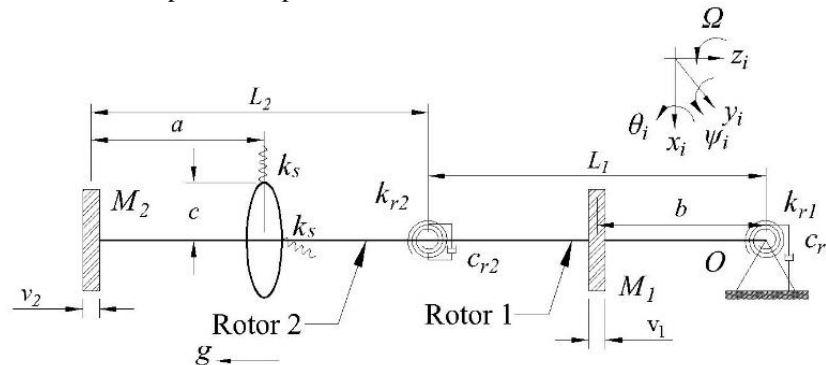


Figure 1. Drawing of the mathematical model.

The acceleration due to gravity acts in the z axis as shown in **Figure 1**. The angles ψ_1 , θ_1 , ψ_2 , and θ_2 are the rotational coordinates of disc 1 and disc 2. The equations of motion were derived using Lagrange equation by deriving the kinetic energy, potential energy and non-conservative forces. The entire mechanical system can be represented using equation (1).

$$[M]\ddot{\vec{u}} + \Omega[G]\dot{\vec{u}} + [C]\dot{\vec{u}} + [K]\vec{u} = \vec{F}_e + \vec{F}_i \quad (1)$$

where \vec{u} is the vector column with the stationary coordinates defined in (2), $[M]$, $[G]$, $[C]$, and $[K]$ represent the mass, gyroscopic, damping, and stiffness matrix, Ω is the rotational speed of the motor, \vec{F}_e is the excitation vector which contains the excitation due to the mass imbalance of each disc, which is derived from the kinetic energy according to [6] and \vec{F}_i represents the impacts between rotor 2 and the stator. The upper dot represents the derivative with respect to time.

$$\vec{u} = [\psi_1 \quad \theta_1 \quad \psi_2 \quad \theta_2]^T \quad (2)$$

The equations of motion were nondimensionalized in order to transform the system into the dimensionless domain, in which the behavior of different physical systems can conveniently be compared. The following nondimensional quantities can be defined as

$$\begin{aligned} \hat{b} &= \frac{b}{L_1}, \quad \hat{a} = \frac{a}{L_1}, \quad \mu_L = \frac{L_1}{L_2}, \quad \mu_d = \frac{d_1}{d_2}, \quad \mu_M = \frac{M_1}{M_2}, \quad \mu_1 = \frac{d_1}{L_1}, \quad \mu_2 = \frac{d_2}{L_2}, \quad \mu_k = \frac{k_{r1}}{k_{r2}}, \quad \mu_{v1} = \frac{v_1}{L_1}, \quad \mu_{v2} = \frac{v_2}{L_2} \\ \bar{\omega}_1 &= \sqrt{\frac{k_{r1}}{M_1 L_1^2}}, \quad \bar{\omega}_2 = \sqrt{\frac{k_{r2}}{M_2 L_2^2}}, \quad \hat{\Omega} = \frac{\Omega}{\bar{\omega}_2}, \quad \tau = \bar{\omega}_2 t, \quad \hat{g} = \frac{g}{L_2 \bar{\omega}_2^2}, \quad \alpha_1 = \frac{e_1}{h}, \quad \alpha_2 = \frac{e_2}{h}, \quad \hat{c} = \frac{c}{h}, \quad \beta = \frac{k_s L_2^2}{k_{r2}}, \\ \hat{\theta}_1 &= \theta_1 \left(\frac{L_1}{h} \right), \quad \hat{\theta}_2 = \theta_2 \left(\frac{L_1}{h} \right), \quad \hat{\psi}_1 = \psi_1 \left(\frac{L_1}{h} \right), \quad \hat{\psi}_2 = \psi_2 \left(\frac{L_1}{h} \right), \quad \hat{r} = \frac{r}{h} \end{aligned}$$

where h is an equivalent radial clearance, which is the projection of c on to the transverse xy plane at $z=L_1+L_2-a$ defined in (3).

$$h = \frac{L_1}{L_1 + L_2 - a} c \quad (3)$$

The coefficient r is the radial displacement of the second rotor at the stator length a which is defined in (4).

$$r^2 = (L_1 \sin \psi_1 + (L_2 - a) \sin \psi_2)^2 + (L_1 \sin \theta_1 + (L_2 - a) \sin \theta_2)^2 \quad (4)$$

Thus, equation (1) can be transformed into the dimensionless domain as shown in equation (5).

$$[\hat{M}]\hat{\ddot{\vec{u}}} + \hat{\Omega}[\hat{G}]\hat{\dot{\vec{u}}} + [\hat{C}]\hat{\dot{\vec{u}}} + [\hat{K}]\hat{\vec{u}} = \hat{\vec{F}}_e + \hat{\vec{F}}_i \quad (5)$$

The matrix $[\hat{M}]$, $[\hat{G}]$, $[\hat{C}]$, and $[\hat{K}]$ are the dimensionless mass, gyroscopic, damping, and stiffness matrix which are shown in Appendix A, defined in (A.1) - (A.4) and the vector $\hat{\vec{F}}_e$ and $\hat{\vec{F}}_i$ are the dimensionless excitation vectors due to the mass imbalance of each disc and due to the impacts between rotor 2 and the stator which are shown in Appendix A, defined in (A.5) and (A.6). The vector column with the nondimensional stationary coordinates is defined in (6).

$$\hat{\vec{u}} = [\hat{\psi}_1 \quad \hat{\theta}_1 \quad \hat{\psi}_2 \quad \hat{\theta}_2]^T \quad (6)$$

The equation of motion that describes the entire dynamical system in equation (5) is now transformed from the stationary frame to the rotating frame, according to [6]. The following transformations are applied.

$$\hat{\vec{u}} = [\hat{T}]\hat{\hat{\vec{u}}} \quad (7)$$

where $[\hat{T}]$ is the nondimensional transformation matrix defined in (8) and $\hat{\hat{\vec{u}}}$ is the nondimensional vector in the rotational coordinate system.

$$[\hat{T}] = \begin{bmatrix} \cos \hat{\Omega} \tau & -\sin \hat{\Omega} \tau & 0 & 0 \\ \sin \hat{\Omega} \tau & \cos \hat{\Omega} \tau & 0 & 0 \\ 0 & 0 & \cos \hat{\Omega} \tau & -\sin \hat{\Omega} \tau \\ 0 & 0 & \sin \hat{\Omega} \tau & \cos \hat{\Omega} \tau \end{bmatrix} \quad (8)$$

Differentiating equation (7) with respect to the nondimensional time τ , with $[\hat{T}]$ defined in equation (8) gives (9) and (10).

$$\hat{\hat{\dot{\vec{u}}}} = [\hat{T}]\hat{\hat{\dot{\vec{u}}}} + [\dot{\hat{T}}]\hat{\hat{\vec{u}}} \quad (9)$$

$$\hat{\hat{\ddot{\vec{u}}}} = [\hat{T}]\hat{\hat{\ddot{\vec{u}}}} - \hat{\Omega}^2 \hat{\hat{\vec{u}}} + 2[\dot{\hat{T}}]\hat{\hat{\dot{\vec{u}}}} \quad (10)$$

According to [6], the following simplification defined in (11) applies to the transformation matrix

$$[\hat{T}]^T [\dot{\hat{T}}] = [\dot{\hat{T}}][\hat{T}]^T = -\hat{\Omega}[\hat{J}] \quad (11)$$

where $[J]$ is shown in (12)

$$[J] = \begin{bmatrix} 0 & 1 & 0 & 0 \\ -1 & 0 & 0 & 0 \\ 0 & 0 & 0 & 1 \\ 0 & 0 & -1 & 0 \end{bmatrix} \quad (12)$$

Applying equations (7), (9), and (10) in equation (5) and multiplying by the transpose of (8) on both sides of equation (5), gives equation (13) in the rotating frame.

$$[\hat{M}] \hat{\ddot{u}} + (-2[\hat{M}][J]\hat{\Omega} + [\hat{G}]\hat{\Omega}) \hat{\dot{u}} + [\hat{C}] \hat{\dot{u}} + ([\hat{K}] - [\hat{M}]\hat{\Omega}^2 - [\hat{C}][J]\hat{\Omega} - [\hat{G}][J]\hat{\Omega}^2) \hat{u} = \hat{F}_e + \hat{F}_i \quad (13)$$

The advantage of converting the equations of motion from the stationary frame to the rotating frame is to clearly identify the contribution of each parameter in the dynamics of a rotating nonlinear system. The term $2[\hat{M}][J]\hat{\Omega}$ represents the Coriolis acceleration and the term $[\hat{M}]\hat{\Omega}^2$ represents the centripetal softening.

Experimental approach

The experimental testing configuration is shown in **Figure 2** (a), which consists of two discs and two rotors connected by isotropic helical couplings. Impacts occur on rotor 2 with a stator positioned at a given height from the wireless sensor, two bearings are attached on rotor 2 to reduce friction forces during contact between the stator and the rotor, as shown in **Figure 2** (b). A brushless electric motor with integrated electronics BLDC58-50L is positioned at the top to give the rotational speed to the dynamical system. The voltage is controlled using National Instruments (NI) cRio-9024 data acquisition system with output module NI-9263. The BLDC58-50L has an embedded system that monitors the speed of the motor, this signal is acquired using input module NI-9215 on FPGA architecture in LabView software. To measure the vibrations of the stator during impact a PCB triaxial accelerometer 356A02 is attached on top of the stator and the signal is acquired using an input module NI-9234. To measure the lateral displacements at the end of rotor 2 a Lord Microstrain triaxial wireless accelerometer G-Link-200-8G is attached and the signal is acquired using Lord Microstrain WSDA-Base-101-LXRS gateway in conjunction with SensorConnect software for the wireless sensor configuration and data acquisition.

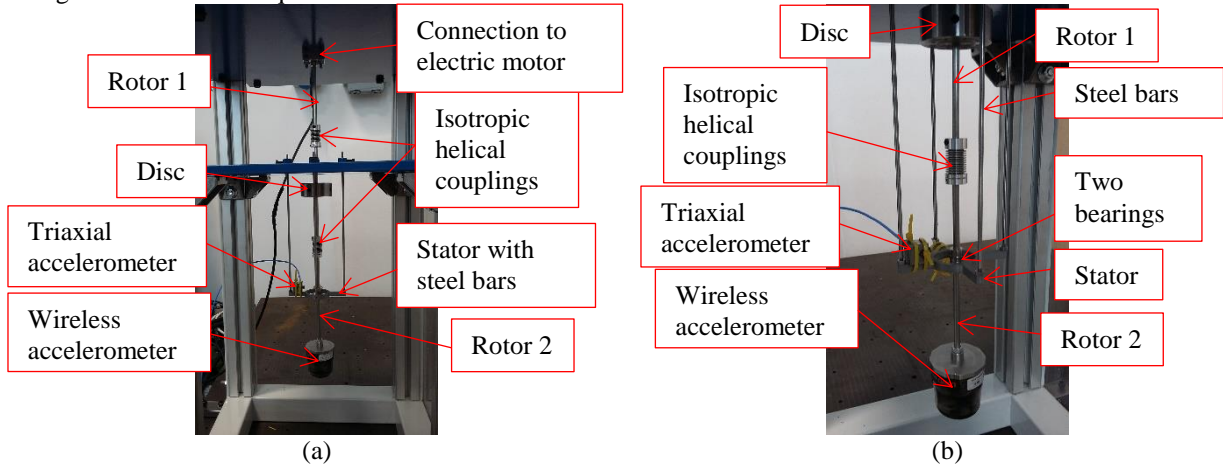


Figure 2 (a) Experimental testing configuration (b) Rotor-stator contact arrangement.

Initial tests were conducted to characterise the underlying linear responses of the system. This will be used to make approximate predictions of drive speeds that will activate sustained asynchronous bouncing motions of the shaft, following the insights in [4]. Testing will be conducted to reproduce sustained asynchronous bouncing motion by exciting the system while it is being driven at a given speed.

To determine the stiffness of the couplings preliminary testing was conducted on one coupling by attaching a rotor at each end of the coupling, rotor 1 was clamped to a fixed support and rotor 2 was free to vibrate like a simple pendulum, as shown in **Figure 3**. A series of testing was conducted by attaching different masses of $M_{tot}=2.44\text{kg}$, 1.44kg , and 0.98kg to the upper part of rotor 2 close to the helical coupling as shown in **Figure 3**, the measured rotor length was $l=0.14\text{m}$ and assuming the gravity is $g=9.81\text{m/s}^2$.

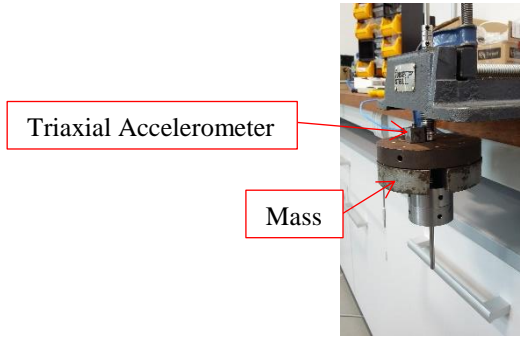


Figure 3 Setup to estimate stiffness and modal damping ratio of helical coupling.

A triaxial shear accelerometer was positioned at the mass to measure the acceleration response. The maximum frequency peak from the FFT spectrum in x and y direction was 2.25Hz - 2.23Hz, as shown in **Figure 4** with $M_{tot}=2.44\text{kg}$, used in equation (14) to calculate the helical coupling stiffness, where ω is the natural frequency of the system.

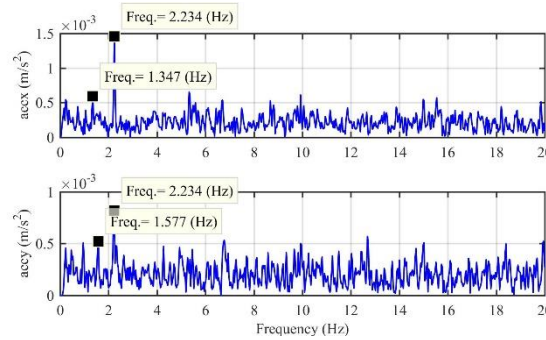


Figure 4 Acceleration response of single pendulum free to vibrate when displaced for test 1 and 2 with $M_{tot}=2.44\text{kg}$ in x and y direction.

$$\omega^2 = \frac{k_{r1}}{l^2 M_{tot}} + \frac{g}{l} \quad (14)$$

The estimated stiffness of the helical coupling was $k_{r1}=k_{r2}=5.90\text{Nm}$. The first peak that appears in **Figure 4** of 1.35Hz - 1.58Hz is coming from the natural frequency of the pendulum when the helical coupling stiffness is neglected. Estimating the natural frequency of the single pendulum with equation (14) taking into account g/l , the natural frequency is 1.33Hz.

The modal damping ratio was also estimated by using the logarithmic decrement technique with the acceleration response after eliminating the DC offset, applying a band pass filter between the frequencies of 2.00Hz – 2.50Hz, and a Hanning Window. The estimated modal damping ratio of the helical coupling was $\zeta_1 = \zeta_2 = 0.02$.

Simulation

The simulation involves the model shown in **Figure 1**. The parameters taken to analyse the dynamic performance of the double rotor system consist of disc 1 and disc 2 with a diameter of $d_1=d_2=46\text{mm}$ and a thickness of $v_1=v_2=19\text{mm}$, the length of both rotors is $L_1=0.333\text{m}$ and $L_2=0.257\text{m}$, the total mass considered is $M_1=0.28\text{kg}$ and $M_2=0.42\text{kg}$. Disc 1 is positioned at the mid span length of rotor 1 and disc 2 is positioned at the bottom end of rotor 2. The stator is positioned at a height from disc 2 of $a=84\text{mm}$ with a radial clearance $c=21\text{mm}$ from the stator ring to the bearings of rotor 2 and the stiffness of the stator is assumed as $k_s=391.6\text{N/m}$. The mass imbalance on disc 1 is assumed to be $e_1=0\text{mm}$ and on disc 2 is assumed to be $e_2=2\text{mm}$. The estimated rotational stiffness of the helical couplings is $k_{r1}=k_{r2}=6.0\text{Nm}$ with an estimated modal damping ratio of $d_{r1}=d_{r2}=0.02$. The gravity is assumed to be $g=9.81\text{m/s}^2$. The simulation time span considered is from 0s to 60.0s.

The equations of motion are solved numerically using Runge-Kutta 4th order; an event detection function is used to locate changes between contact and non-contact motion. Once the contact has been established the resulting force of excitation can be calculated during contact.

A Campbell diagram is shown in **Figure 5** in the stationary frame to demonstrate the variation of the linear natural frequencies versus the rotor speed. In **Figure 5**, the red lines represent the forward whirl, the blue lines represent the backward whirl of the rotors, and the dashed green line represent the rotor speed. The linear natural frequencies can be estimated by obtaining the eigenvalues with the characteristic equation defined in (15), where the vector λ represents the eigenvalues of the stiffness matrix $[\hat{K}]$ defined in (A.4), the gyroscopic matrix $[\hat{G}]$ defined in (A.2), the mass matrix $[\hat{M}]$ defined in (A.1), and the rotor speed $\hat{\Omega}$.

$$\det\left(\left[\hat{K}\right]-\lambda\left[\hat{G}\right]\hat{\Omega}+\lambda^2\left[\hat{M}\right]\right)=0 \quad (15)$$

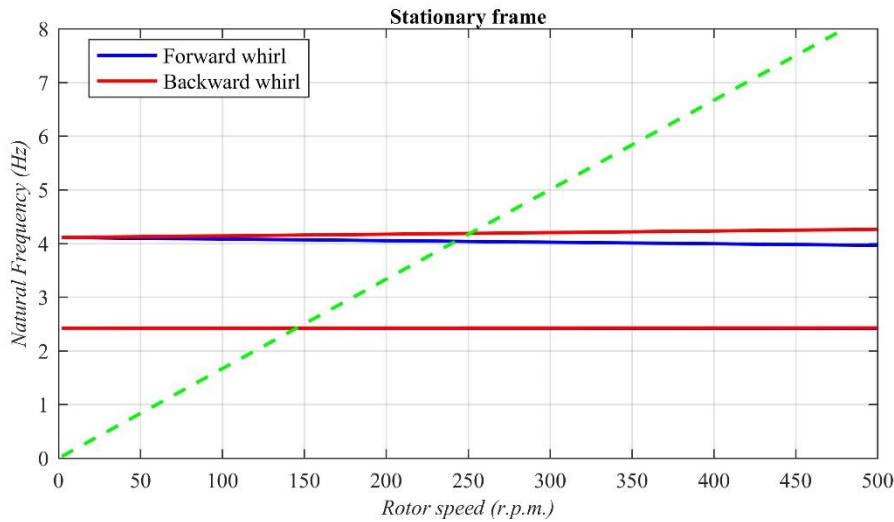


Figure 5 Campbell diagram of the double rotor system where the blue lines represent the backward whirl, the red lines represent the forward whirl, and the dashed green line represent the rotor speed.

The crossings between the rotor speed and the linear natural frequencies of the rotors determine the critical speeds of the dynamical system, according to [6] where resonance will occur. The critical speeds of the system can be determined from **Figure 5** which are 144 r.p.m., 242 r.p.m., and 254 r.p.m. In **Figure 5** can be seen that the first forward and backward whirl are identical due to the effect of the gyroscopic terms.

The variation of the natural frequencies versus the rotor speed in the rotating frame is shown in **Figure 6**, where the red lines represent the forward whirl and the blue lines represent the backward whirl of the rotors. The natural frequencies in the rotating frame can be estimated by obtaining the eigenvalues with the characteristic equation defined in (16), where the vector λ represent the eigenvalues of the stiffness matrix $[K]$ defined in (A.4), the gyroscopic matrix $[G]$ defined in (A.2), the mass matrix $[M]$ defined in (A.1), and the rotor speed $\hat{\Omega}$.

$$\det\left(\left([\hat{K}]-[\hat{M}]\hat{\Omega}^2-[\hat{G}][J]\hat{\Omega}^2\right)-\lambda\left(-2[\hat{M}][J]\hat{\Omega}+[\hat{G}]\hat{\Omega}\right)+\lambda^2[\hat{M}]\right)=0 \quad (16)$$

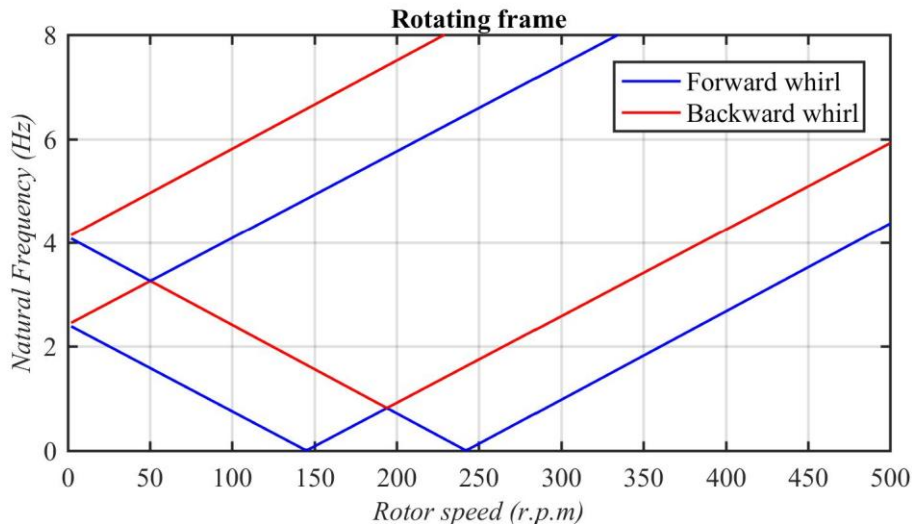


Figure 6 Natural frequencies in the rotating frame of the double rotor system where the blue lines represent the backward whirl and the red lines represent the forward whirl.

A brute force bifurcation is developed according to [4] to study the model due to the discontinuous nonlinearity by conducting several time-domain simulations. The bifurcation diagram shown in **Figure 7** reveals the bouncing orbits at supercritical drive speeds. The bifurcation diagram in **Figure 7** was done by developing a range of simulations conducted with different rotor speeds from 0 r.p.m. to 500 r.p.m. The set of angular initial conditions considered is 0 rad, 0.2 rad, 0.4 rad, 0.6 rad, 0.8 rad, and 1.0 rad each initial condition is placed to rotor 1, rotor 2 individually and to both rotors simultaneously in the x axis for each rotor speed. The steady state part of the orbit r_2 was determined at the stator height a and the maximum values from each rotor speed and initial conditions were obtained.

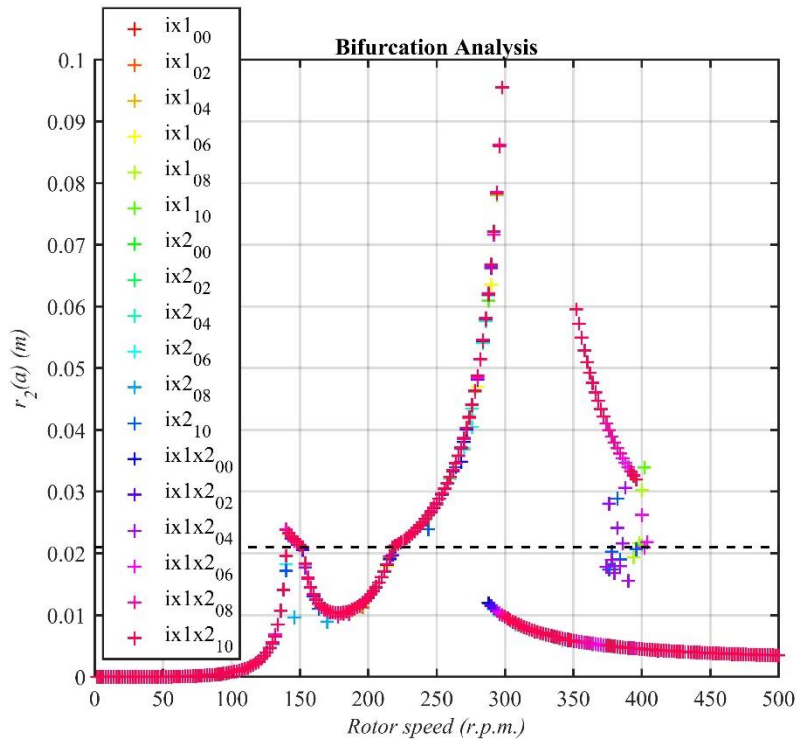


Figure 7 Bifurcation diagram by brute force for a range of different initial conditions the dashed black line represents the stator radial clearance and the color cross are the different initial conditions considered.

All cases shown in **Figure 7** settle to synchronous whirling motion where the radial displacement of the stator node remains constant. In **Figure 7** the first peak at 142 r.p.m. corresponds to the first critical speed of the system in the stationary frame. The motion up until 350 r.p.m. is either linear forward whirl (non-contacting) or in the case of the higher amplitude oscillations between 140 r.p.m. - 150 r.p.m. and again between 222 r.p.m. - 298 r.p.m a constant contact forward whirl occur. The linear forward whirl can also exist as a possible stable solution between 290 r.p.m. - 350 r.p.m. and between 406 r.p.m - 500 r.p.m.

The asynchronous bouncing-type partial contact motion start to occur at 350 r.p.m. to 402 r.p.m. depending on the initial condition considered. The idea is to reproduce this asynchronous partial contact motion using the experimental test rig described in the previous section.

The best simulation results to demonstrate the asynchronous bouncing-type partial contact motions are obtained when considering the initial condition of 1.0 rad applied in the x axis to rotor 1 and rotor 2 simultaneously with a rotor speed of 352 r.p.m.

In **Figure 8** (a) and **Figure 9** (a) is shown the orbits of rotor 1 and rotor 2 at L_1 and L_2 respectively, between the time span of 45.0 s and 58.0 s in the stationary frame at the rotor speed of 352 r.p.m. shows that while the motion seems orderly it is not periodic in the stationary frame; the orbit shown will continually precess each other. In **Figure 8** (b) and **Figure 9** (b) is shown the orbits of rotor 1 and rotor 2 at L_1 and L_2 respectively, between the time span of 45.0s and 58.0s in the rotating frame at the rotor speed of 352 r.p.m. shows the periodic motion of rotor 1 and rotor 2 when viewed in the rotating frame.

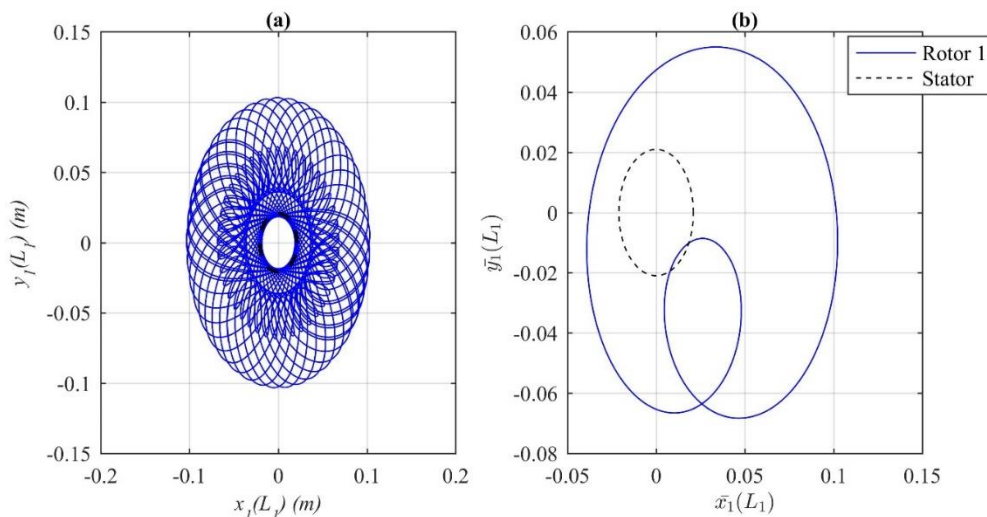


Figure 8 Steady-state partial contact orbit of rotor 1 at drive speed 352 r.p.m. between the time span of 45.0s and 58.0s, the dashed black line is the stator clearance (a) Partial contact orbit in the stationary frame. (b) Partial contact orbit in the rotating frame.

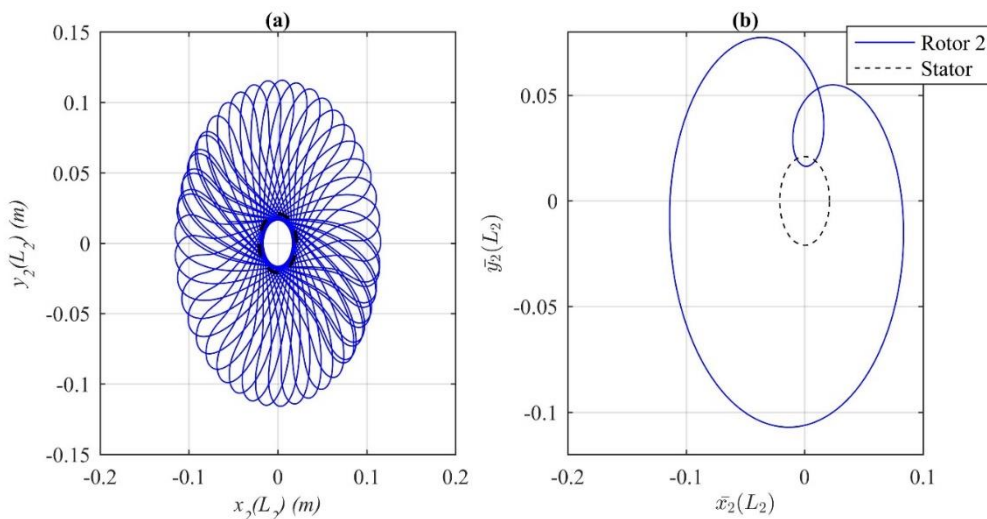


Figure 9 Steady-state partial contact orbit of rotor 2 at drive speed 352 r.p.m. between the time span of 45.0s and 58.0s, the dashed black line is the stator clearance (a) Partial contact orbit in the stationary frame. (b) Partial contact orbit in the rotating frame.

In **Figure 10** shows the radial displacement of rotor 2 over the entire time span represented by a blue line and the stator radial clearance is represented by a dashed black line. From **Figure 10** is obtained the maximum displacement of the steel bars attached to the stator under the impacts of rotor 2 which is approximately 4.6 cm. The high displacements of the steel bars at the stator are due to the low stiffness assumed in the simulation.

In **Figure 11** is shown the Poincaré maps sampled at the drive frequency (Ω) for rotor 2 at L_2 between the time span of 45.0 s and 58.0 s at (a) in the stationary frame and at (b) in the rotating frame when the rotor speed is 352 r.p.m. In **Figure 11** (a) the rotor motion in the stationary frame is not periodic. However, in the rotating frame shown in **Figure 11** (b) the orbit is periodic.

The mathematical model presented gives the response of a double rotor system to be able to predict and reproduce in an experimental test rig the asynchronous bouncing type partial contact motion of the rotor when impacts occur with a stator. Future work is currently plan to validate the simulation results with the experimental results obtained from the test rig described earlier to be presented.

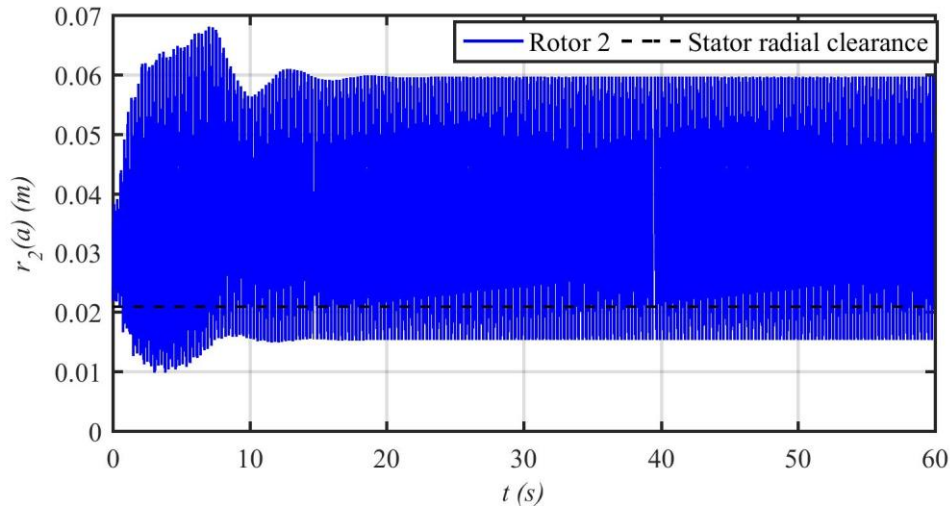


Figure 10 Radial displacement of rotor 2 at the height of the stator the blue line represents the rotor radial displacement and the dashed black line represent the stator radial clearance.

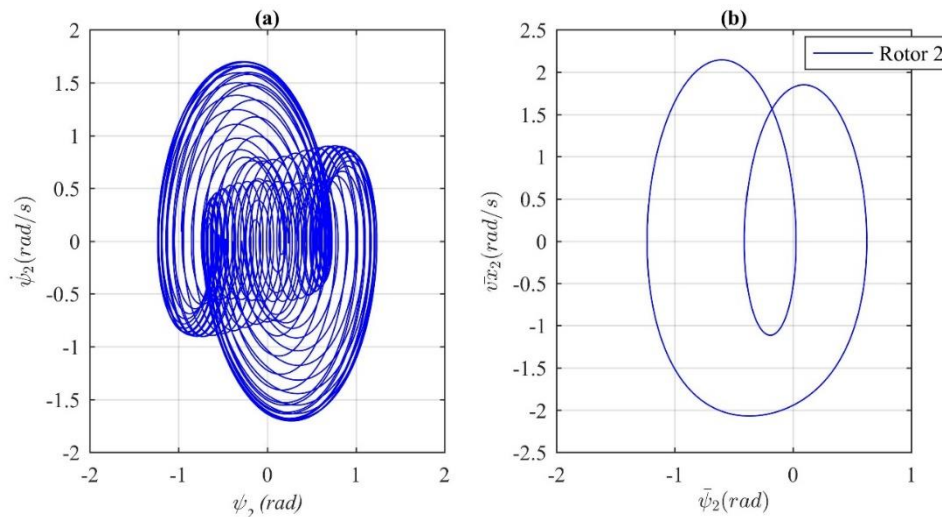


Figure 11 Poincaré maps of rotor 2 at drive speed 352 r.p.m. between the time span of 45.0s and 58.0s (a) In the stationary frame with respect to ψ_2 . (b) In the rotating frame with respect to θ_2 .

Conclusion

The equations of motion in the rotating frame of a double rotor system with isotropic helical couplings with discs attached at a given length of the rotors, where a rotor can impact with a stator positioned at a given length of a rotor, are derived in this paper. These equations accommodate the nonlinear effects due to impact between the stator and the rotor which accommodate the quadratic coupling terms, a 2:1 internal resonance takes place, which result in the asynchronous bouncing type partial contact motion of the rotor. A description of the experimental test rig was presented. The approach used to determine the stiffness and modal damping ratio of the helical couplings was demonstrated. The parameters determined experimentally were used in the simulation to demonstrate the partial contact motion of the rotor. In the future work the asynchronous bouncing type partial contact motion of the double rotor system predicted with the mathematical model will be validated with the experimental test rig presented in this paper.

Acknowledgement

The research presented in this paper is funded from the Engineering and Physical Sciences Research Council (EPSRC) grant “Engineering Nonlinearity” EP/G036772/1 is gratefully acknowledged.

Appendix A

The dimensionless mass, gyroscopic, damping, and stiffness matrix $[\hat{M}]$, $[\hat{G}]$, $[\hat{C}]$, and $[\hat{K}]$ are defined in (A.1) - (A.4).

$$[\hat{M}] = \begin{bmatrix} \mu_M \mu_L \hat{b}^2 + \frac{\mu_M \mu_d^2 \mu_2^2}{16 \mu_L} + \mu_L + \frac{\mu_M \mu_{v1}^2 \mu_L}{12} & 0 & 1 & 0 \\ 0 & \mu_M \mu_L \hat{b}^2 + \frac{\mu_M \mu_d^2 \mu_2^2}{16 \mu_L} + \mu_L + \frac{\mu_M \mu_{v1}^2 \mu_L}{12} & 0 & 1 \\ \mu_L & 0 & 1 + \frac{\mu_2^2}{12} + \frac{\mu_{v2}^2}{12 \mu_L} & 0 \\ 0 & \mu_L & 0 & 1 + \frac{\mu_2^2}{12} + \frac{\mu_{v2}^2}{12 \mu_L} \end{bmatrix} \quad (\text{A.1})$$

$$[\hat{G}] = \begin{bmatrix} 0 & -\frac{\mu_M \mu_L \mu_1^2}{8} & 0 & 0 \\ \frac{\mu_M \mu_L \mu_1^2}{8} & 0 & 0 & 0 \\ 0 & 0 & 0 & -\frac{\mu_2^2}{8} \\ 0 & 0 & \frac{\mu_2^2}{8} & 0 \end{bmatrix} \quad (\text{A.2})$$

$$[\hat{C}] = \begin{bmatrix} 2\zeta_1 \sqrt{\mu_k \mu_M} \hat{b}^2 + 2\zeta_2 \mu_L & 0 & 2\zeta_2 & 0 \\ 0 & 2\zeta_1 \sqrt{\mu_k \mu_M} \hat{b}^2 + 2\zeta_2 \mu_L & 0 & 2\zeta_2 \\ 2\zeta_2 \mu_L & 0 & 2\zeta_2 & 0 \\ 0 & 2\zeta_2 \mu_L & 0 & 2\zeta_2 \end{bmatrix} \quad (\text{A.3})$$

$$[\hat{K}] = \begin{bmatrix} \hat{b}^2 \frac{\mu_k}{\mu_L} + \mu_L + \mu_M \hat{b} \hat{g} + \hat{g} & 0 & 1 & 0 \\ 0 & \hat{b}^2 \frac{\mu_k}{\mu_L} + \mu_L + \mu_M \hat{b} \hat{g} + \hat{g} & 0 & 1 \\ \mu_L & 0 & 1 + \hat{g} & 0 \\ 0 & \mu_L & 0 & 1 + \hat{g} \end{bmatrix} \quad (\text{A.4})$$

The dimensionless excitation vector due to the mass imbalance of each disc \hat{F}_e is defined in (A.5).

$$\hat{F}_e = \begin{bmatrix} \mu_M \mu_L \alpha_1 \hat{b} \hat{\Omega}^2 \\ 0 \\ \alpha_2 \hat{\Omega}^2 (\mu_L + 1) \mu_L \\ 0 \end{bmatrix} \quad (\text{A.5})$$

The dimensionless vector due to the impacts between rotor 2 and the stator \hat{F}_i is defined in (A.6). The coefficient $H(\hat{p})$ is a penalty function defined in (A.7).

$$\hat{F}_i = \begin{bmatrix} 0 \\ 0 \\ H(\hat{p}) \beta \left(1 - \frac{\hat{c}}{\hat{r}}\right) (\mu_L + 1 - \mu_L \hat{a}) \left((\mu_L \hat{\psi}_1 + (1 - \mu_L \hat{a}) \hat{\psi}_2) \cos \hat{\Omega} \tau + (\mu_L \hat{\theta}_1 + (1 - \mu_L \hat{a}) \hat{\theta}_2) \sin \hat{\Omega} \tau \right) \\ H(\hat{p}) \beta \left(1 - \frac{\hat{c}}{\hat{r}}\right) (\mu_L + 1 - \mu_L \hat{a}) \left(-(\mu_L \hat{\psi}_1 + (1 - \mu_L \hat{a}) \hat{\psi}_2) \sin \hat{\Omega} \tau + (\mu_L \hat{\theta}_1 + (1 - \mu_L \hat{a}) \hat{\theta}_2) \cos \hat{\Omega} \tau \right) \end{bmatrix} \quad (\text{A.6})$$

$$H(\hat{p}) = \begin{cases} \|\hat{r}_2(a)\| - \hat{c} \geq 0; H(\hat{p}) = 1 \\ \|\hat{r}_2(a)\| - \hat{c} < 0; H(\hat{p}) = 0 \end{cases} \quad (\text{A.7})$$

Reference

- [1] E. V. Karpenko, M. Wiercigroch, and M. P. Cartmell, “Regular and chaotic dynamics of a discontinuously nonlinear rotor system,” *Chaos, Solitons and Fractals*, vol. 13, no. 6, pp. 1231–1242, 2002.
- [2] D. Zilli, Andrea; Williams, Robin J; Ewins, David J. “Non-linear Dynamics of a Simplified Model of an Overhung Rotor Subjected to Intermittent Annular Rubs,” in *ASME Turbo Expo 2014: Turbine Technical Conference and Exposition GT2014*, 2014, pp. 1–13.
- [3] L. Salles, B. Staples, N. Hoffmann, and C. Schwingshackl, “Continuation techniques for analysis of whole aeroengine dynamics with imperfect bifurcations and isolated solutions,” *Nonlinear Dynamics*, vol. 86, no. 3, pp. 1–15, 2016.
- [4] A. D. Shaw, A. R. Champneys, M. I. Friswell, F. Way, and S. Sa, “Asynchronous partial contact motion due to internal resonance in multiple rotordynamics,” in *Proceeding of the Royal Society*, 2016, pp. 1–25.
- [5] W. Qin, G. Chen, and G. Meng, “Nonlinear responses of a rub-impact overhung rotor,” *Chaos, Solitons and Fractals*, vol. 19, no. 5, pp. 1161–1172, 2004.
- [6] M. I. Friswell, J. E. T. Penny, S. D. Garvey, and A. W. Lees, *Dynamics of Rotating Machines*. 2010.